



HAL
open science

**Polar stratospheric cloud microphysical properties
measured by the microRADIBAL instrument on 25
January 2000 above Esrange and modeling
interpretation**

C. Brogniez, N Huret, S. Eckermann, E. Riviere, Michel Pirre, M. Herman,
J.-y Balois, C. Verwaerde, N. Larsen, B. Knudsen

► **To cite this version:**

C. Brogniez, N Huret, S. Eckermann, E. Riviere, Michel Pirre, et al.. Polar stratospheric cloud microphysical properties measured by the microRADIBAL instrument on 25 January 2000 above Esrange and modeling interpretation. *Journal of Geophysical Research: Atmospheres*, 2003, 108 (D6), pp.15. 10.1029/2001JD001017. insu-02878964

HAL Id: insu-02878964

<https://insu.hal.science/insu-02878964>

Submitted on 23 Jun 2020

HAL is a multi-disciplinary open access archive for the deposit and dissemination of scientific research documents, whether they are published or not. The documents may come from teaching and research institutions in France or abroad, or from public or private research centers.

L'archive ouverte pluridisciplinaire **HAL**, est destinée au dépôt et à la diffusion de documents scientifiques de niveau recherche, publiés ou non, émanant des établissements d'enseignement et de recherche français ou étrangers, des laboratoires publics ou privés.

Polar stratospheric cloud microphysical properties measured by the microRADIBAL instrument on 25 January 2000 above Esrange and modeling interpretation

C. Brogniez,¹ N. Huret,² S. Eckermann,³ E. D. Rivière,² M. Pirre,² M. Herman,¹ J.-Y. Balois,¹ C. Verwaerde,¹ N. Larsen,⁴ and B. Knudsen⁴

Received 2 July 2001; revised 16 May 2002; accepted 27 May 2002; published 20 March 2003.

[1] The balloonborne microRADIBAL instrument is a radiometer that measures the radiance and polarization of the sunlight scattered by the atmosphere, gas, and aerosols in a horizontal plane in the near-infrared range. It was launched from Esrange, Sweden, on 25 January 2000 in the framework of the Third European Stratospheric Experiment on Ozone (THESEO) 2000 campaign, and performed measurements in the vicinity of a large polar stratospheric cloud (PSC). The measurements provide diagrams of the radiance versus scattering angle at several altitudes. The aerosol signature, derived from the radiance measurements, has been modeled via Mie theory and the T-Matrix code. Three different size distributions of aerosols have been tested: monomodal and bimodal size distributions of spherical particles, and bimodal size distributions including a mode of spherical and a mode of nonspherical particles. The best agreement between the measured and modeled signatures is obtained considering a bimodal size distribution composed by a mode of medium spherical particles (median radius about 0.15 μm) and a second mode of larger nonspherical particles (median radius about 1.1 μm , aspect ratio about 0.6). Concentrations and surface densities of the PSC particles have been estimated. The existence of such particles has been tentatively explained using the Lagrangian Microphysical and Photochemical Lagrangian Stratospheric Model of Ozone (MiPLaSMO) model. On 25 January 2000 the polar stratospheric cloud detected by microRADIBAL is associated with a lee-wave event. Temperature perturbations due to lee-wave events were calculated using the National Research Laboratory Mountain Wave Forecast Model (MWFM) and have been included along trajectories. They are localized in a large region between the Norwegian mountains and Esrange. Their amplitude varies from 3 to 7 K. Detailed comparisons between measured and modeled surfaces and dimensional distributions of PSCs' particles are achieved. The two modes of particles detected by microRADIBAL can be interpreted from MiPLaSMO results considering different air masses located along the lines of sight. The air masses are characterized by two different temperature perturbations due to lee-wave events. With a small temperature perturbation (~ 3 K) that occurred just before the time of the measurement, supercooled ternary solution particles are predicted, and with a strong temperature perturbation (~ 6 K) that occurred four hours before the measurement, nitric acid trihydrate particles are formed. *INDEX TERMS:* 0305 Atmospheric Composition and Structure: Aerosols and particles (0345, 4801); 0320 Atmospheric Composition and Structure: Cloud physics and chemistry; 0341 Atmospheric Composition and Structure: Middle atmosphere—constituent transport and chemistry (3334); 0360 Atmospheric Composition and Structure: Transmission and scattering of radiation

¹Laboratoire d'Optique Atmosphérique, Centre Nationale de Recherche Scientifique, Université des Sciences et Technologies de Lille, Villeneuve d'Ascq, France.

²Laboratoire de Physique et Chimie de l'Environnement, CNRS, Université d'Orléans, Orléans, France.

³E. O. Hulburt Center for Space Research, Naval Research Laboratory, Washington D. C., USA.

⁴Danish Meteorological Institute, Copenhagen, Denmark.

Citation: Brogniez, C., N. Huret, S. Eckermann, E. D. Rivièrè, M. Pirre, M. Herman, J.-Y. Balois, C. Verwaerde, N. Larsen, and B. Knudsen, Polar stratospheric cloud microphysical properties measured by the microRADIBAL instrument on 25 January 2000 above Esrange and modeling interpretation, *J. Geophys. Res.*, 108(D6), 8332, doi:10.1029/2001JD001017, 2003.

1. Introduction

[2] It is now well known that polar stratospheric clouds (PSCs) play a crucial role in the polar ozone loss by activating chlorine species and/or by denitrifying the atmosphere. The understanding and the quantification of the impact of such clouds on ozone chemistry is one of the objectives of the scientific community [*World Meteorological Organization (WMO)*, 1999]. The knowledge of these clouds has evolved considerably since early studies [*Steele et al.*, 1983; *Toon et al.*, 1989; *Crutzen and Arnold*, 1986; *Hamill and Toon*, 1991] thanks to many laboratory and in situ measurements. Nevertheless, a lot of uncertainties are still remaining concerning their composition, phase, size distribution, and formation conditions. Three kinds of PSC particles are usually considered: ice particles, solid nitric hydrate particles (nitric acid trihydrate (NAT) or nitric acid dihydrate (NAD)) and supercooled ternary solutions (STS). The laboratory study of *Koop et al.* [1997] suggests us the existence windows for each kind of particles as a function of temperature. The temperature range where the NAT phase is stable, overlaps with the STS existence temperature range in the neighborhood of the NAT saturation temperature, T_{NAT} . During the Arctic winter 1999 *Schreiner et al.* [1999] detected the presence of liquid particles consistent in composition with supercooled ternary solutions rather than solid hydrates, for low temperature between 189 and 192 K associated with a lee-wave event. But in January 2000 the same instrument has revealed successively the presence of NAT particles and the presence of STS particles [*Voigt et al.*, 2000] associated with small temperature fluctuations. The temperature perturbations due to mesoscale lee-wave event are a nonnegligible pathway of solid particles formation in Arctic region [*Carslaw et al.*, 1999]. Moreover, *Larsen et al.* [1997] have shown that PSC 1a particles (solid particles according to optical classification, probably composed of NAT), can be formed when air masses experiment a long residence time below T_{NAT} (not necessary below T_{ICE}) at synoptic scale. Thus in Arctic region the air mass temperature histories have to be studied in detail at both synoptic scale and mesoscale to describe PSC formation and interpret the in situ measurements.

[3] The extensive field campaign, THESEO 2000, dedicated to the study of the polar atmosphere, took place in winter 2000 from Kiruna, Sweden. The balloonborne instrument microRADIBAL, developed by the Laboratoire d'Optique Atmosphérique (LOA) to observe stratospheric aerosols, flew during this campaign. It is a miniaturized version of RADIBAL, developed also by LOA in the 1980's, which observed the stratospheric aerosols many times in previous experiments and has been used for satellite measurement cross validations [*Ackerman et al.*, 1989; *Brogniez et al.*, 1992, 1996, 1997; *Santer et al.*, 1992]. It belongs to a category of instruments performing sparse measurements dedicated to aerosol characterization in specific conditions. These instruments use various techniques such as those developed in particle counters [*Deshler*

et al., 1993; *Ovarlez and Ovarlez*, 1995], aerosol lidars [*Flentje et al.*, 2000], and occultation instruments [*Renard et al.*, 2000]. MicroRADIBAL measures the sunlight scattered by the atmosphere in various directions, from which information on the aerosol phase function, and therefore on the aerosol size distribution can be derived. It performed its first scientific flight on 25 January 2000, from Esrange-Kiruna (Sweden) while PSCs were clearly observed from the ground.

[4] In this study, the MiPLaSMO model has been run along isentropic trajectories to interpret the data obtained by the microRADIBAL instrument. This model allows us to follow the time evolution of a population of particles influenced by microphysical processes (nitric acid and water condensation/evaporation, freezing of STS) using thermodynamic calculations. Then surface areas can be deduced for the three different kinds of PSC particles [*Rivièrè et al.*, 2000].

[5] The instrument and the measurements are described in section 2, as well as the data processing and the retrieved aerosol characteristics. Section 3 details the Lagrangian model, MiPLaSMO, along with the lee-wave modeling and the trajectory studies leading to the particle characterization. The consistency between the observed and modeled aerosol characteristics is discussed in section 4.

2. MicroRADIBAL Measurements

2.1. Description

[6] MicroRADIBAL was developed by the LOA during 1998/1999. It is a modified version of the photopolarimeter RADIBAL (RADIomètre BALlon) [*Herman et al.*, 1986] that can be flown on a stratospheric platform. The instrument has been miniaturized, to allow an easier launch without an auxiliary balloon, and has been upgraded: the measurements are performed in 5 channels (instead of 2 in RADIBAL) centered in the near infrared at 730 nm (full width at half maximum = 10 nm), 865 nm (55 nm), 1000 nm (40 nm), 1270 nm (80 nm) and 1620 nm (65 nm). The three first channels are equipped with silicium detectors while the two others are InGaAs detectors cooled by a one stage Peltier module. The new instrument is composed of 15 separate optics whose axes are parallel, with narrow fields of view ($\text{FOV} = 1.5^\circ$). They are arranged in groups of 3 for each wavelength, the 3 optics being equipped with analyzers positioned 60° one from each other in order to derive the polarized light.

[7] The radiometers detect the sunlight scattered by the atmosphere (gas and particles) and an absolute calibration in the laboratory (via an integrated sphere calibrated every year by Labsphere Laboratory, traceable to the National Institute for Standards and Technology (NIST)) enables radiance and degree of polarization of the scattered sunlight to be inferred. Owing to the rotation of the gondola around its vertical axis, the observations are performed under various directions in a horizontal plane. Scans are thus

obtained with an angular sampling of about $2\text{--}6^\circ$ depending on the rotation rate. A magnetometer allows us to determine the azimuth direction of the line of sight and to deduce the corresponding scattering angle with respect to the solar incident light.

[8] Note that, accounting for the measurement method (horizontal viewing), the detectors integrate the signal from the balloon to a distance of about $100\text{--}300$ km (depending on the aerosol density profile). One must also bear in mind that due to the FOV of the instrument (1.5°), the width of the region observed at 200 km is about 5 km. Moreover, for the different scattering angles, the measurements correspond to light coming from various azimuth directions, and thus from different geographical locations.

[9] The microRADIBAL instrument was launched from Esrange ($67.9^\circ\text{N}/22.1^\circ\text{E}$), Sweden, at $09:00$ UT on 25 January 2000 since a PSC was clearly observed from the ground. The measurements are usually performed during the ascent or the descent of the balloon, and the aerosol are studied at several altitudes. During this flight, due to trajectory constraints, measurements were made during the ascent of the balloon. Due to some problems in the flight train (twisting of the train) the gondola sometimes rotated very fast and thus only sequences in the $17\text{--}21$ km range could be used. The $17\text{--}21$ km altitude level was reached at about $10:00$ UT, the balloon position being about $66.7^\circ\text{N}/22^\circ\text{E}$.

[10] As in previous RADIBAL analyses [Herman *et al.*, 1986; Santer *et al.*, 1988, 1992; Brogniez *et al.*, 1992, 1996, 1997] in each channel we consider the radiance L normalized to the solar irradiance E outside Earth's atmosphere, i.e., the reflectance

$$\rho(\theta) = \frac{\pi L(\theta)}{E}, \quad (1)$$

where θ is the scattering angle. The reference irradiance, E , in the 730 nm and 865 nm channels is derived from Fröhlich and London [1986], in the other channels it is derived from Arvesen *et al.* [1969]. The normalized radiance is studied as reflectance diagrams.

2.2. Data Processing

[11] In order to eliminate the impact of the oscillations of the gondola (leading to variations in the optical thickness of the observed air mass), the diagrams have been smoothed over 5° scattering angle range and averaged over about 300 m altitude range. To retrieve the scattering characteristics of the aerosols, the molecular contribution has to be removed from the measurements, as will be explained below. Because of the polarizing properties of the molecules, their relative contribution to the polarized radiance is much larger than their relative contribution to the total radiance. Since the molecular contribution is evaluated by assuming an horizontal viewing, any failure in the smoothing process entails large errors in the polarized light. The polarization data proved to be too noisy and they have not been used in the following analysis.

[12] Figure 1 shows the averaged reflectance measurements obtained at about 20 km. The solar azimuth is 170° , and the positive scattering angles correspond to observations toward the Scandinavian mountains, whereas the negative scattering angles are associated to regions located

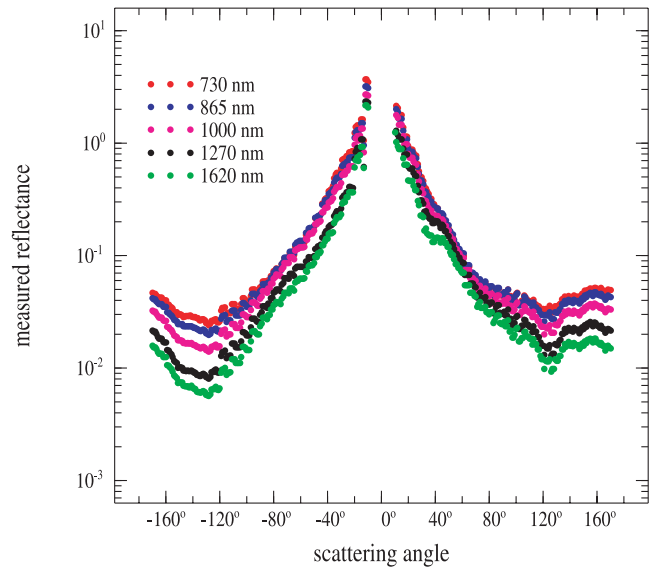


Figure 1. Reflectance measurements versus scattering angle, obtained at about 20 km altitude by microRADIBAL in the five channels. The sign of the scattering angle is to distinguish observations on both sides of the solar incident plane.

eastward of the balloon. Despite the averaging, one can notice that the diagram is asymmetric with respect to the solar incident plane. The aerosols of the polar stratosphere have been observed by RADIBAL during several previous flights performed in winter from Esrange. A typical example of these measurements, obtained in a free-PSC stratosphere in February 1997, is reported in Figure 2. We first observe that the reflectance is $5\text{--}10$ times larger in January 2000 than in the February 1997 flight. In a comparison between these measurements two characteristics clearly appear: (1) there is a strong variation from forward to backward scattering angles, much larger in the 2000 measurements than in no-PSC conditions, (2) the spectral variations, from 865 nm to 1620 nm, are weaker in 2000 than during no-PSC observations for about the same wavelengths, especially in the forward direction. These measurements show that the situation encountered on 2000 is more complicated than previous ones in free PSC atmosphere. Then, in the present study we choose, in a first approach, to interpret measurements associated with positive scattering angles.

[13] To analyze the measurements, the reflectance in each channel is expressed in the single scattering approximation as follows [Santer *et al.*, 1988]

$$\rho_\lambda(\theta) = \frac{t_\lambda(\theta)}{4} \left\{ \delta_{\lambda,\text{aer}} \left(p_{\lambda,\text{aer}}(\theta) + 2\rho_{\lambda,\text{g}} \sinh_s \right) + \delta_{\lambda,\text{Rayl}} \left(p_{\text{Rayl}}(\theta) + 2\rho_{\lambda,\text{g}} \sinh_s \right) \right\}, \quad (2)$$

where t is the atmospheric transmission from the sun to the detectors, δ is the slant optical thickness, p is the phase function, ρ_{g} is the reflectance of the atmosphere or ground below the balloon and h_s is solar elevation. The indices

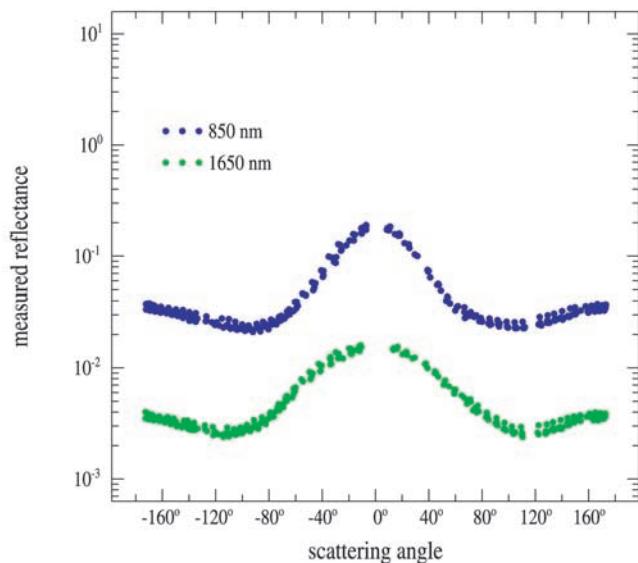


Figure 2. Same as Figure 1 but for a RADIBAL flight performed on 9 February 1997. Only two channels were available.

“aer” and “Rayl” refer to aerosols and Rayleigh respectively. The Rayleigh slant optical thickness is derived from the temperature and pressure profiles available from the PTU sounding performed by the Swedish Space Corporation-Esrange (09:29 UT) close to the balloon trajectory. Estimation of the surface reflectance $\rho_{\lambda,g}$ has been obtained from several previous RADIBAL flights (1994–1995–1997) conducted from Esrange over snowed lands, by using a reflectance-meter. We observed little variability in these data from flight to flight. As the small microRADIBAL gondola was not equipped with a reflectance-meter, we took for $\rho_{\lambda,g}$ mean values of those previous measurements. Note that the solar elevation was low during the flight ($h_s \sim 4^\circ$) so that the term due to the surface is rather small.

[14] The data processing here was different from the usual RADIBAL flight processing to make the aerosol signature more obvious. We first remove the molecular and the surface contributions from the measured reflectance to derive a term that we call “corrected reflectance”:

$$\rho_\lambda^{\text{corr}}(\theta) = \frac{\rho_\lambda(\theta)}{t_\lambda(\theta)} - \frac{\delta_{\lambda,\text{Rayl}}}{4} \left(p_{\text{Rayl}}(\theta) + 2\rho_{\lambda,g} \sinh_s \right), \quad (3)$$

which corresponds to the aerosol signature

$$\rho_\lambda^{\text{corr}}(\theta) = \frac{\delta_{\lambda,\text{aer}}}{4} \left(p_{\lambda,\text{aer}}(\theta) + 2\rho_{\lambda,g} \sinh_s \right). \quad (4)$$

By assuming that the transmission t_λ is equal to 1 in equation (3), a first fit to the spectral and angular variations of the aerosol signature (equation (4)), via Mie theory for lognormal (LND) size distributions, allows us to estimate the aerosol phase function in each channel; the aerosol slant optical thickness is then expressed as:

$$\delta_{\lambda,\text{aer}} = 4 \frac{\rho_\lambda^{\text{corr}}(\theta)}{p_{\lambda,\text{aer}}(\theta) + 2\rho_{\lambda,g} \sinh_s}; \quad (5)$$

then the transmission is derived following *Santer et al.* [1988], and new values of $\rho_\lambda^{\text{corr}}(\theta)$ are derived according to equation (3).

[15] These corrected reflectances are modeled using equation (4) via a radiative transfer code. The data processing relies on the analysis of the directional and spectral behaviors, and the aerosol size distribution allowing to retrieve these behaviors is inferred.

[16] The spectral aerosol extinction coefficients, $\sigma_{\lambda,\text{ext}}$ at the balloon altitude z are derived from the slant optical thickness measurements by assuming that the aerosol layer, here the PSC, is homogeneous and located in a small height range Δh above z , which gives the approximate formula

$$\sigma_{\lambda,\text{ext}} \approx \delta_{\lambda,\text{aer}} \sqrt{\frac{1}{2R\Delta h}}, \quad (6)$$

where R is the Earth radius.

[17] Δh has been estimated using POAM III (Polar Ozone and Aerosol Measurements) measurements obtained three hours later, 300 km apart from the balloon. POAM III has observed large extinction corresponding to a PSC layer around 20 km, about 3–6 km thick. In our case, because microRADIBAL instrument was within the PSC, we have set Δh to a smaller range (1.5–3 km) than POAM III estimate. With these values equation (6) leads to $\sigma_{\lambda,\text{ext}}$ in the $0.005\delta_{\lambda,\text{aer}} - 0.009\delta_{\lambda,\text{aer}}$ range. For each wavelength two limit values of the extinction coefficient are then derived.

[18] Finally, given these measured extinction coefficients and the estimated extinction cross section of the particles for the retrieved size distribution, the number density and the surface area density ranges of the aerosols are derived.

2.3. Results

[19] We have simulated the “corrected reflectance” (equation (4)) for various aerosol models and the best model has been determined with a least squares fit method, by minimizing the mean relative error, AE, computed over the angular range and the five channels, i.e., N values, according to the expression

$$\text{AE} = \sqrt{\frac{1}{N} \sum_{\lambda=1}^5 \sum_{\theta} \left[\frac{\rho_\lambda^{\text{corr,mod}}(\theta) - \rho_\lambda^{\text{corr,meas}}(\theta)}{\rho_\lambda^{\text{corr,mod}}(\theta)} \right]^2}, \quad (7)$$

where the indices “meas” and “mod” are for measured and modeled signals respectively.

[20] We have first considered the simple case of a monomodal LND size distribution of spherical particles. A large set of LND size distributions, characterized by their median radius (r_m) and their geometric standard deviation (σ), has been tested. The corresponding effective radii range between 0.05–1.5 μm . We used Mie theory for spherical aerosols of fixed refractive index; a mean constant value equal to 1.43 has been selected since the total radiance measurements are not much sensitive to this parameter.

[21] Since various measurements have already shown that bimodal size distributions were observed in the stratosphere [see, e.g., *Deshler and Oltmans, 1998*], we have also investigated if a combination of two modes of spherical particles could lead to a better agreement. The size distri-

Table 1. Characteristics of the Best Models Selected at 20 km for the Three Types of Size Distributions and Mean Errors^a

Model	r_{m1} , μm	σ_1	$r_{\text{eff}1}$, μm	r_{m2} , μm	σ_2	$r_{\text{eff}2}$, μm	AE, %
One mode: spherical particles (M1)	0.25	1.73	0.53				11.6
Two modes: spherical particles (M2)	0.15	1.82	0.37	0.75	1.65	1.4	13
Two modes: spherical + nonspherical particles (M3)	0.15	1.82	0.37	1.1 ^b	1.35	1.38	9

^aWhere r_{mi} is median radius, σ_i is geometric standard deviation, r_{eff} is effective radius, and ε is aspect ratio.

^bWhere $\varepsilon = 0.6$.

butions accounted for two LND components of spherical particles, varying the parameters, r_m and σ , of the two modes and their relative concentration.

[22] Considering the low temperature values, available from the PTU sounding close to the balloon (193 K at level 20 km), which suggest us that solid particles could exist, we also looked at nonspherical particles. We simulated the measurements with size distributions whose large component is constituted by nonspherical particles characterized by their aspect ratio ε , the smaller component remaining spherical. We used the T-matrix code provided by *Mishchenko et al.* [1996] for particles with effective radius in the 0.6–1.8 μm range.

[23] We will refer hereafter to model 1 (M1), model 2 (M2) and model 3 (M3) for the three cases of particle size distributions considered: one LND of spherical particles, two LND of spherical particles and two LND of spherical and nonspherical particles.

[24] We detail here the results obtained at 20 km. For these measurements (see Figure 1) two features at about 30°–45° and 120°–130° scattering angles exist. They are probably due to very localized microphysical processes. In this preliminary study, we chose to discard them, and focus on the interpretation of the signal obtained over a wider scattering angle range.

[25] The characteristics of the best models selected, according to the AE criterion (see equation (7)), for the three types of size distributions are reported in Table 1, together with the respective mean relative errors. Note that the effective radius, $r_{\text{eff}} = 0.53 \mu\text{m}$ for M1, and $r_{\text{eff}} = 0.37 \mu\text{m}$ for the medium mode of M2 and M3, is much larger than for the background aerosols, r_{eff} about 0.05 μm [Deshler et al., 1993]. The effective radius of the second mode is very large, r_{eff} about 1.4 μm .

[26] Each model leads to a mean relative error about 10% and the best retrieval is obtained with M3 (AE = 9%). We have checked for statistical significance in the changes by applying the Student's t test [Press et al., 1992] (there are 136 measurement points for each of the five wavelengths). The change is not significant between M1 and M2, but the improvements are significant to the 5% level for M1/M3 and for M2/M3.

[27] To investigate whether a directional heterogeneity exists, we have also performed fits over smaller angular ranges 10°–70°, 70°–115° and 135°–175° and compared the results in each angular range to the results obtained previously. The mean relative errors are similar, no significant improvement is obtained and for the three angular ranges the aerosol model the most satisfying is the same model M3. We have checked that the corresponding slant optical thickness, derived from equation (5) and needed to the number density calculations, are very close to the values obtained from the global fit. Therefore we can conclude that

we do not observe a directional heterogeneity, and a global fit over the whole angle range is satisfying.

[28] Figure 3 shows the microRADIBAL measurements and the fits for each wavelength obtained with M3. Over all scattering angles a good agreement between measurements and fits is obtained, and there are no significant variations of the mean relative errors as a function of scattering angle.

[29] Thus a size distribution composed of one mode of medium spherical particles and one mode of large nonspherical particles gives a good agreement over a wide angular range, and a unique size distribution ($r_{m1} = 0.15 \mu\text{m}$, $\sigma_1 = 1.82$; $r_{m2} = 1.1 \mu\text{m}$, $\sigma_2 = 1.35$, $\varepsilon = 0.6$), can be considered from 10° to 175° scattering angle.

[30] The aerosol extinction coefficients are computed according to the interval defined from equation (6), and the number densities and surface area densities are derived. We have reported in Table 2, the characteristics of the two particle modes retrieved at 20 km altitude with model M3, and the corresponding densities. Uncertainties in the retrieved modes have been estimated by varying the two modes and their relative concentration without changing much the quality of the fit. The mean relative error obtained is very close to the minimum value obtained for the best fit (within 0.5%). Table 2 reports the values obtained in two

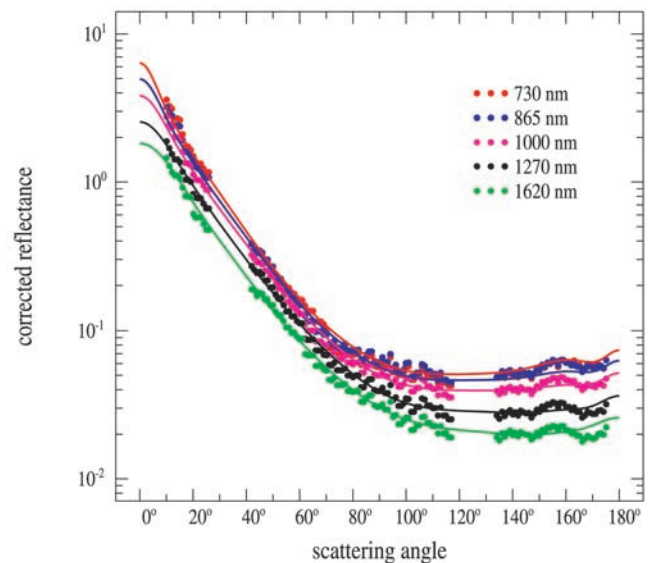


Figure 3. Comparison between the “corrected reflectance” derived from the measurements (dots) and the mean retrieved diagrams (solid lines) obtained with a combination of a size distribution of spherical particles ($r_{m1} = 0.15 \mu\text{m}$, $\sigma_1 = 1.82$), and of a size distribution of non spherical particles ($r_{m2} = 1.1 \mu\text{m}$, $\sigma_2 = 1.35$ with an aspect ratio $\varepsilon = 0.6$).

Table 2. Detailed Characteristics of the Two Modes of Particles Retrieved at 20 km^a

	r_{m1} , μm	σ_1	$r_{\text{eff}1}$, μm	n_1 , cm^{-3}	s_1 , $\mu\text{m}^2\text{cm}^{-3}$	r_{m2} , ^b μm	σ_2 ^b	$r_{\text{eff}2}$, ^b μm	n_2 , cm^{-3}	s_2 , $\mu\text{m}^2\text{cm}^{-3}$
Best fit	0.15	1.82	0.37	13–24	7.5–14	1.1	1.35	1.38	0.05–0.09	0.9–1.8
Limit	0.1	2.0	0.34	28–47	9–16	1.2	1.35	1.5	0.04–0.07	0.8–1.5
Limit	0.2	1.65	0.37	8–14	6.5–11.5	1.0	1.49	1.5	0.06–0.1	1.0–1.7

^aWhere r_{mi} is median radius, σ_i is geometric standard deviation, $r_{\text{eff}i}$ is effective radius, e is aspect ratio, n_i is number density, and s_i is surface area density. The intervals account for uncertainty on the aerosol profile (see section 2.3). The first case is for the “best” fit, while the two last lines correspond to the “limit” cases (see section 2.3).

^bWhere $\varepsilon = 0.6$.

limit cases. The corresponding effective radii of the two modes of the size distributions are close to the previous values as well as the surface areas.

[31] The retrieved characteristics of the aerosols at two other altitudes (17.5 and 21 km) are reported in Table 3. The best agreement is obtained considering the same model M3 as at 20 km, but the mean errors are about 20%.

[32] Finally, microRADIBAL radiance measurements between 17.5–21 km, in the positive scattering angle range, can be retrieved accounting for one mode of medium-sized spherical particles and one mode of larger non spherical particles, whose effective radii are $r_{\text{eff}1} \approx 0.35 \mu\text{m}$ and $r_{\text{eff}2} \approx 1.4 \mu\text{m}$, respectively. At 17.5 km the aerosol number densities of each mode are smaller than at the other altitudes, therefore one can conclude that the bottom of the PSC was located around 17.5 km.

[33] Since the 20 km level has led to better agreement between measurements and modeling from radiative transfer study, we focussed on this layer for the following detailed chemical and microphysical modeling interpretation.

3. Modeling Interpretation

[34] MiPLaSMO is a Lagrangian model devoted to the study of chemical and microphysical processes associated with ozone destruction. This model includes a detailed chemical code involving 125 reactions in gas phase with 10 heterogeneous reactions, describing the time evolution of 42 species, and a detailed microphysical code using thermodynamic calculations [Larsen, 2000].

[35] Along isentropic trajectories, calculated off-line [Knudsen et al., 2001] using ECMWF analyses, the model allows us to follow the time evolution of the aerosol spectrum. Coolings due to mountain waves are calculated off-line by the NRL/MWFM model [Eckermann et al., 1998] and can be included along trajectories. A complete description of the MiPLaSMO model can be found in previous studies [Huret et al., 1998; Rivière et al., 2000].

3.1. MiPLaSMO Microphysical Module Description

[36] The microphysical module considers five types of particles: liquid aerosols (sulfuric aerosols), liquid PSC particles (supercooled ternary solution (STS)), solid aero-

sols (sulfuric acid tetrahydrate (SAT)), solid PSC particles (nitric acid trihydrate (NAT) or Ice). Two pathways are possible for the formation of solid particles from liquid particles. When temperature decreases, initial liquid sulfuric aerosols can grow by condensation of nitric acid and water to form a supercooled ternary solution (STS) [Tabazadeh et al., 1994; Carslaw et al., 1995]. STS particles begin to freeze at $T_{\text{ice}} -1 \text{ K}$ and ice particles are formed. Condensed HNO_3 and H_2SO_4 are conserved through the formation of an inner NAT shell surrounding a SAT core in the ice particles. According to Koop et al. [1997] STS particles can remain liquid until $T_{\text{ice}} -3 \text{ K}$ threshold is reached. Then, if temperature increases, ice evaporates and residual NAT appears. The other pathway allows direct formation of NAT particles, below T_{NAT} , from STS particles by homogeneous freezing, following the parameterization given by Tabazadeh et al. [2001]. This last process occurs more readily in the air masses that are cooling slowly. NAT and ice PSC can evaporate if the temperature increases and solid aerosols as SAT appear. SAT aerosols can melt if temperature is greater than the melting point of SAT, T_{melt} [Middlebrook et al., 1993] or deliquesce if temperature decreases and the concentration of nitric acid in gas phase is sufficient to form STS [Koop and Carslaw, 1996]. Nucleation of NAT particles on SAT aerosols is also possible on pre-activated SAT aerosols [Zhang et al., 1996].

3.2. Meteorological Conditions on 25 January 2000

[37] We have successively investigated the formation of the PSC detected by microRadibal at synoptic scale and at mesoscale. Detailed analyses of temperature histories based on ECMWF analysis and on NRL/MWFM results for synoptic scale and mesoscale respectively, are provided together with MiPLaSMO results.

3.2.1. Synoptic Scale

[38] As mentioned previously in 2.2, the aerosol extinction coefficients are computed according to equation (6), and then the number densities and surface areas are derived. With the maximum value taken for Δh , about 3 km, that means that information is coming from up to about 200 km. A cluster of ten day backward trajectories has been calculated in a region localized on the west side of the instru-

Table 3. Characteristics of the Two Particle Types of the “Best” Retrievals at 17.5 and 21 km Altitude^a

Z, km	r_{m1} , μm	σ_1	n_1 , cm^{-3}	s_1 , $\mu\text{m}^2\text{cm}^{-3}$	r_{m2} , ^b μm	σ_2 ^b	n_2 , cm^{-3}	s_2 , $\mu\text{m}^2\text{cm}^{-3}$
17.5	0.15	1.82	6.5–10.5	3.5–6.5	1.1	1.35	0.02–0.04	0.3–0.7
21	0.15	1.82	18–29	10.5–17	1.1	1.35	0.09–0.15	1.6–2.7

^aNotations are as in Table 2.

^bWhere $\varepsilon = 0.6$.

ment, corresponding to microRADIBAL measurements with positive scattering angles. This region is defined between the neighborhood of the microRADIBAL instrument (66.7N, 22.1 E) and a boundary about 200 km far from the instrument.

[39] In this entire region temperature histories of the air masses deduced from ECMWF analyses are similar. Figure 4a shows the time evolution of the temperature T_{ECMWF} for the air mass corresponding to the neighborhood of microRADIBAL instrument at 20 km. The time scale is given in hours: time = 0h corresponds to the time of the measurements on 25 January 2000 at 10:00 UT, time = -240h corresponds to 15 January 2000 at 10:00 UT (the beginning of the trajectory 10 days before the measurements). The time evolution of T_{ice} , T_{NAT} and T_{melt} calculated along the trajectory has also been plotted on the graph, with concentrations of 5 ppmv for water vapor and 10 ppbv for nitric acid. Figure 4a shows that T_{ECMWF} is warmer than T_{melt} 100 hours before the time of the measurement. A cooling appears 20 hours before the time of measurement, but temperature never decreases below T_{ice} , and temperature at the time of measurement is above T_{ice} and below T_{NAT} .

[40] Time evolution of aerosol surface area, predicted by MiPLaSMO along the trajectory, is presented in Figure 4b. Surface areas corresponding to the two types of particles measured by microRADIBAL are also shown (stars with error bars).

[41] Initial particles are considered to be liquid sulfuric aerosols, which is consistent with the temperature history where $T_{ECMWF} > T_{melt}$ 100 hours before the end of the trajectory (Figure 4a). The characteristics of the initial lognormal spectrum are taken from measurements of the University of Wyoming Optical Particle Counter (UW-OPC) [Deshler *et al.*, 1993] on 19 January 2000 available from the NILU (Norwegian Institute for Air Research) database. For this level the median radius is $r_m = 0.029 \mu\text{m}$, the standard deviation $\sigma = 1.6$, and the total number of particles $N = 12.8 \text{ cm}^{-3}$.

[42] During the cooling that appears 20 hours before the measurements, liquid aerosols grow by condensation of nitric acid and water and STS occurs with a maximum surface $s = 7 \mu\text{m}^2/\text{cm}^3$. Then the temperature increases, STS fully evaporates and liquid sulfuric aerosols are predicted. Liquid sulfuric aerosol surface area predicted by MiPLaSMO ($s = 0.25 \mu\text{m}^2/\text{cm}^3$) at the time of measurements corresponds to background aerosols initially present in the air mass, with a smaller surface than the surface of the first type of particles measured by microRADIBAL ($s = 6.5\text{--}16 \mu\text{m}^2/\text{cm}^3$). The second type of particles detected by the instrument cannot be reproduced by the model when using only the temperature history given by ECMWF analyses at synoptic scale. In this case, the only microphysical process that occurs in the air masses is condensation/evaporation of nitric acid and water on initial liquid sulfuric aerosols. Direct freezing of STS particles into NAT particles described by Tabazadeh *et al.* [2001] does not occur, because the residence time of the air mass below T_{NAT} is too short.

[43] However, Carslaw *et al.* [1998], Berendt [2000] and Rivière *et al.* [2000] have shown that temperature perturbations due to lee-wave events in the Arctic often need to be taken into account to interpret correctly microphysical

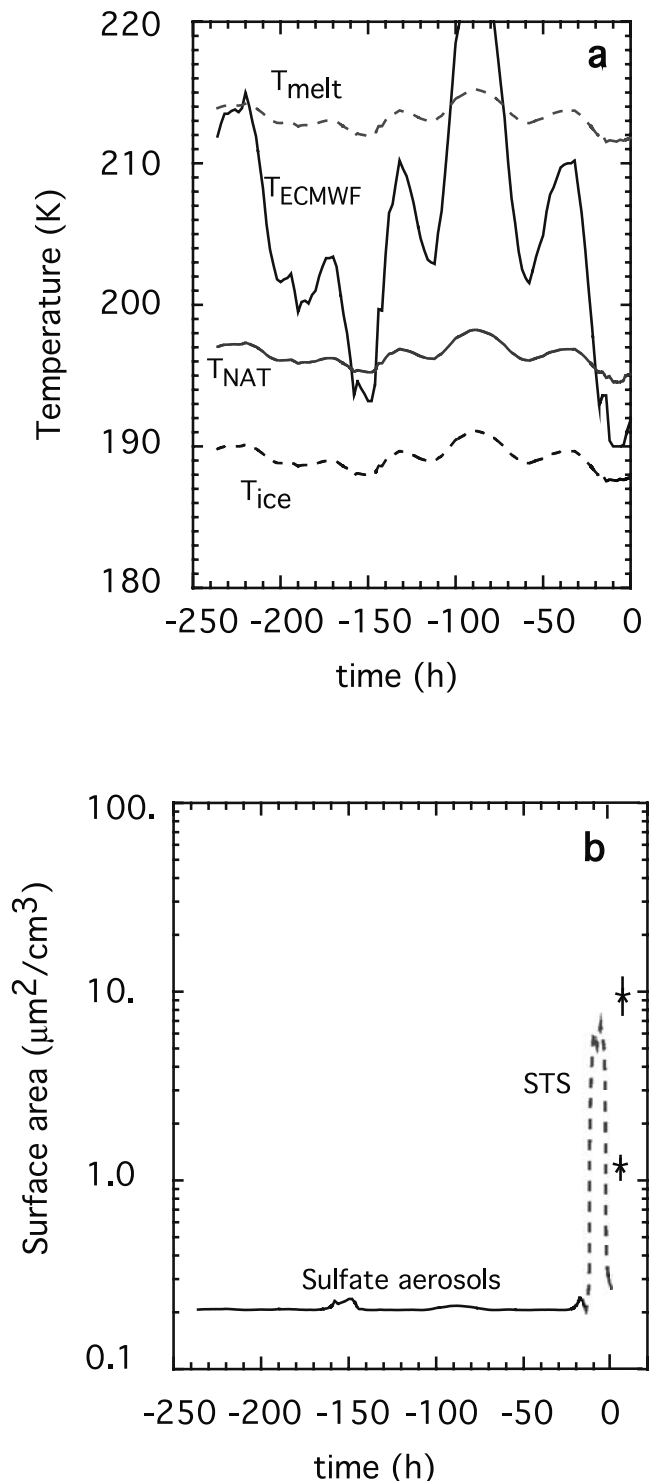


Figure 4. (a) Synoptic temperature (T_{ECMWF}) time evolution for the 10-days back trajectory (heavy solid line) at the 20 km altitude for 25 January 2000. Melting temperature of SAT (T_{melt}), temperature of NAT condensation (T_{NAT}), and ice frost point (T_{ice}) are also shown; $t = 0\text{h}$ corresponds to the time of the measurements. (b) Simulated time evolution of the particle surface area for liquid particles, and at $t = 0\text{h}$ surface areas for the two particle modes measured by microRADIBAL (stars).

measurements over orography. In the next section, temperature perturbations due to lee-wave events are investigated.

3.2.2. Mesoscale Temperature Fluctuations

[44] Mountain-wave effects on this day were assessed by performing hind-cast simulations with version 2.0 of the Mountain Wave Forecast Model (MWFM), a nonhydrostatic ray-based extension of the hydrostatic 1.0 model initially developed by *Bacmeister et al.* [1994]. MWFM 2.0 was used to provide operational forecasts of stratospheric mountain-wave activity throughout the SOLVE/THESEO 2000 mission, and proved fairly successful in forecasting and diagnosing various stratospheric mountain-wave events that arose during the 1999/2000 winter [*Hertzog et al.*, 2002; S. D. Eckermann et al., unpublished manuscript, 2002].

[45] Hind-cast results here use NASA Data Assimilation Office (DAO) $1^\circ \times 1^\circ$ analyses for 25 January 2000 as the background atmosphere for the MWFM model. Rather than plotting the multiray results directly, as was done for on-site forecasts and detailed wave case studies [e.g., *Hertzog et al.*, 2002], here we use an averaged hemispheric product with the same $1^\circ \times 1^\circ$ gridding as the global DAO analysis. This product was developed specifically to assess the role of mountain-wave mesoscale temperature fluctuations (MTFs) within the global photochemical transport model experiments of *Pierce et al.* [2002]. Briefly, hind-cast MWFM ray results within each $1^\circ \times 1^\circ$ DAO grid box at each pressure level were averaged to provide an average peak temperature amplitude and standard deviation due to the various mountain waves within this volume.

[46] Grid box-averaged peak temperature amplitudes (ΔT_{MTF}) due to hind-cast mountain waves at 50 hPa over Scandinavia are plotted in Figure 5 at 6:00 UT and 12:00 UT on 25 January 2000. The model forecasts significant mountain wave-induced temperature amplitudes over northern Scandinavia, consistent with detailed analyses of forecasts, models and aircraft/balloon measurements of this region of the stratosphere on this day [e.g., *Dörnbrack et al.*, 2002; *Voigt et al.*, 2000; S. D. Eckermann et al., unpublished manuscript, 2002]. In particular, the map shows significant (reversible) MTF cooling due to mountain waves in the vicinity of Esrange.

[47] The trajectory corresponding to an air mass in the neighborhood of the instrument is plotted in red and an example of a trajectory corresponding to an air mass on the west side of the instrument (about 200 km far from it) is plotted in yellow. The positions of the air masses at 6:00 UT (corresponding to 4 hours before the time of measurements) are illustrated by stars.

[48] Mountain-wave MTFs are localized above the Norwegian mountains and are spatially inhomogeneous: however, it should be noted that mesoscale model simulations suggest some downstream penetration of larger-scale inertially modified waves on this day [*Dörnbrack et al.*, 2002]. The maximum temperature perturbation is around 6 K (yellow region) and the air masses corresponding to the neighborhood of the instrument (red trajectory) crosses this region exactly at 6:00 UT (Figure 5a). The air masses on the west side of the instrument, were located over the sea at 6:00 UT. The MTF map at 12:00 UT (Figure 5b) shows that the region where the lee-wave event occurs has extended on the east side of the Scandinavian mountains, with amplitude

smoothed between north and south. Thus we might reasonably assume that, at 10:00 UT, air masses located on the west side and far from the instrument have experimented temperature perturbations around 3 K.

[49] Given this scenario, two types of temperature histories can be identified, hereafter referred to as Temperature Histories 1 and 2 (TH1 and TH2). For the trajectories leading to the neighborhood of the instrument (TH1), the temperature perturbations are ~ 6 K prior to the measurements, and temperature oscillations exist for ~ 2 hours. For the region located on the west side of the instrument, temperature history 2 (TH2) corresponds to temperature oscillations that begin 2 hours before the time of measurements. The maximum temperature perturbation in this case is ~ 3 K. For both types of temperature histories, the oscillation period is set to 30 min, as by *Tsias et al.* [1997], which is roughly in the range of small-scale intrinsic wave periods inferred for a southern Scandinavian wave event observed on 2 March 2000 by *Hertzog et al.* [2002].

3.3. MiPLaSMO Results

[50] Temperature perturbations due to the hind-cast lee-wave event shown in Figure 5 have been included along trajectories for TH1 and TH2. Figure 6 shows the time evolution of the temperature of the air masses and of the particle surface area, accounting for the two temperature histories defined previously. Surface areas measured by microRADIBAL are also plotted for the two types of particles (stars with error bars). Values of surface areas predicted assuming TH1 are $0.23 \mu\text{m}^2/\text{cm}^3$ for sulfate aerosols and $1.6 \mu\text{m}^2/\text{cm}^3$ for NAT, and, assuming TH2 the predicted surface area is $10 \mu\text{m}^2/\text{cm}^3$ for STS. Values measured by microRADIBAL are $6.5\text{--}16 \mu\text{m}^2/\text{cm}^3$ for spherical particles, and $0.8\text{--}1.8 \mu\text{m}^2/\text{cm}^3$ for nonspherical particles.

[51] For TH1, the temperature perturbations induce a cooling of the air mass below T_{ice} , four hours before measurements (Figure 6a). At the time of measurements temperature is above T_{ice} . During the strong cooling, liquid sulfuric aerosols grow by condensation leading to the formation of STS. Then, when temperature decreases below T_{ice} , a part of these large liquid STS particles freeze to form ice particles. All STS particles are not frozen because the temperature never decreases below $T_{ice} - 3$ K. Then, when temperature increases, ice evaporates and residual NAT particles appear. At the measurement point the air mass contains two types of particles: liquid sulfuric aerosols and NAT particles (Figure 6b). The NAT surface area predicted is consistent with the surface area of the second mode of particles detected by microRADIBAL (lower star). Unfortunately the model cannot reproduce the large surface areas of the first type of particles obtained by the instrument (upper star).

[52] Considering temperature history TH2, during the lee-wave event, the temperature never went below $T_{ice} - 1$ K (Figure 6c). Particles predicted in this case are STS (Figure 6d), and the surface area predicted is in agreement with the first mode of particles measured by microRADIBAL. In this case only one type of particles is predicted by the model.

[53] The modeling calculations show that the type of PSC particles predicted depends strongly on the intensity of the temperature perturbation. STS and NAT particles cannot be

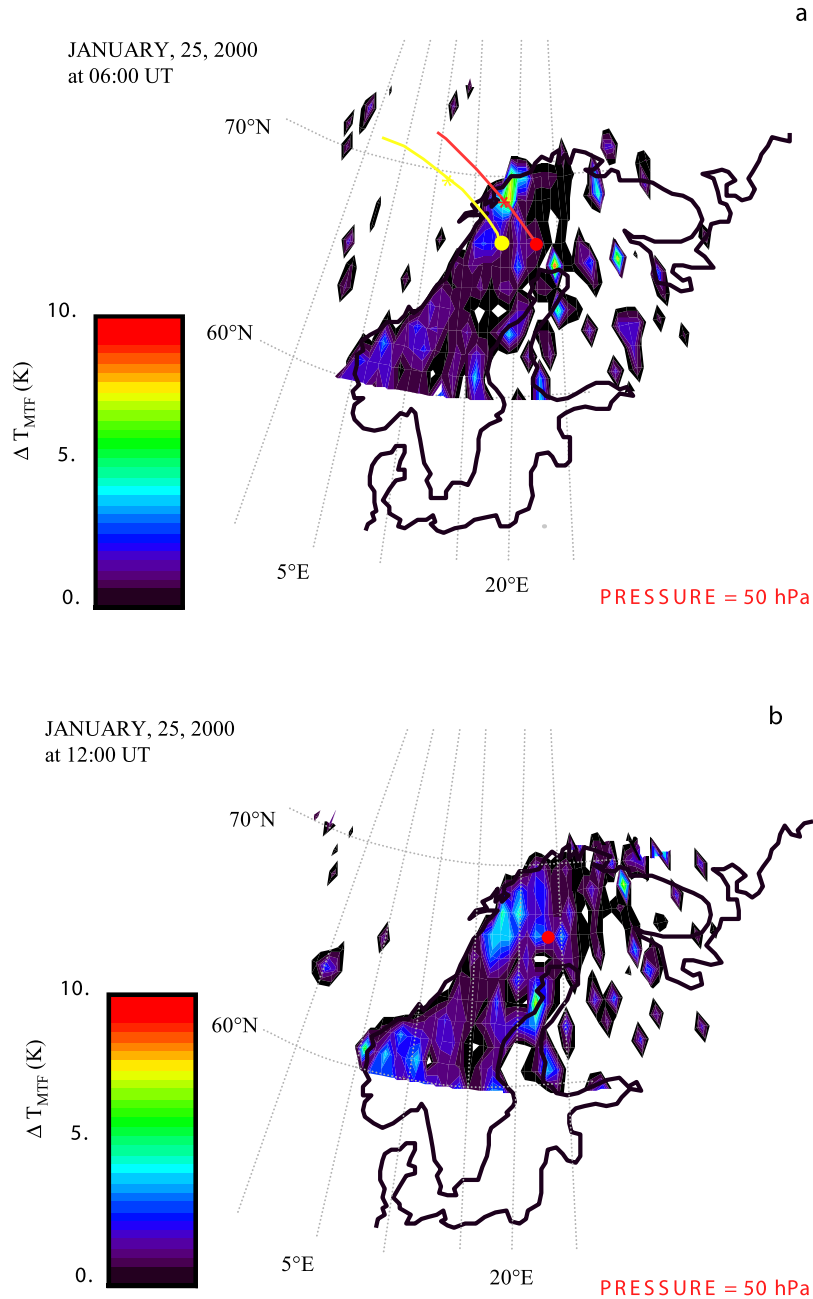


Figure 5. Grid box-averaged peak temperature amplitudes (ΔT_{MTF}) due to hind-cast mountain waves at 50 hPa over Scandinavia at 6:00 UT (a) and 12:00 UT (b) on 25 January 2000. ΔT_{MTF} is the amplitude of the temperature perturbation due to lee-wave event with respect to the synoptic temperature analysis (T_{ECMWF}). The red dot indicates the balloon position. Air mass trajectories corresponding to the neighborhood of the balloon (red) and to west side of the balloon (yellow) are drawn. In Figure 5a, stars correspond to the air mass locations at 6:00 UT.

predicted in the same air mass at the same time. MWFM model has highlighted two temperature histories, corresponding to different air masses explored by microRADIBAL, located in the neighborhood of the balloon and far from it. In the first case, when the temperature decreases below T_{ice} , NAT particles and small liquid sulfuric aerosols are predicted. In the second case, when the temperature is below T_{NAT} but above T_{ice} at the time of measurement, large STS particles are predicted. STS and NAT particles surface

area predicted by the model are respectively consistent with those obtained for the medium mode of spherical particles and for the large mode of nonspherical particles by microRADIBAL.

4. Discussion

[54] On the one hand, the microRADIBAL analysis shows that the measurements can be explained by assuming

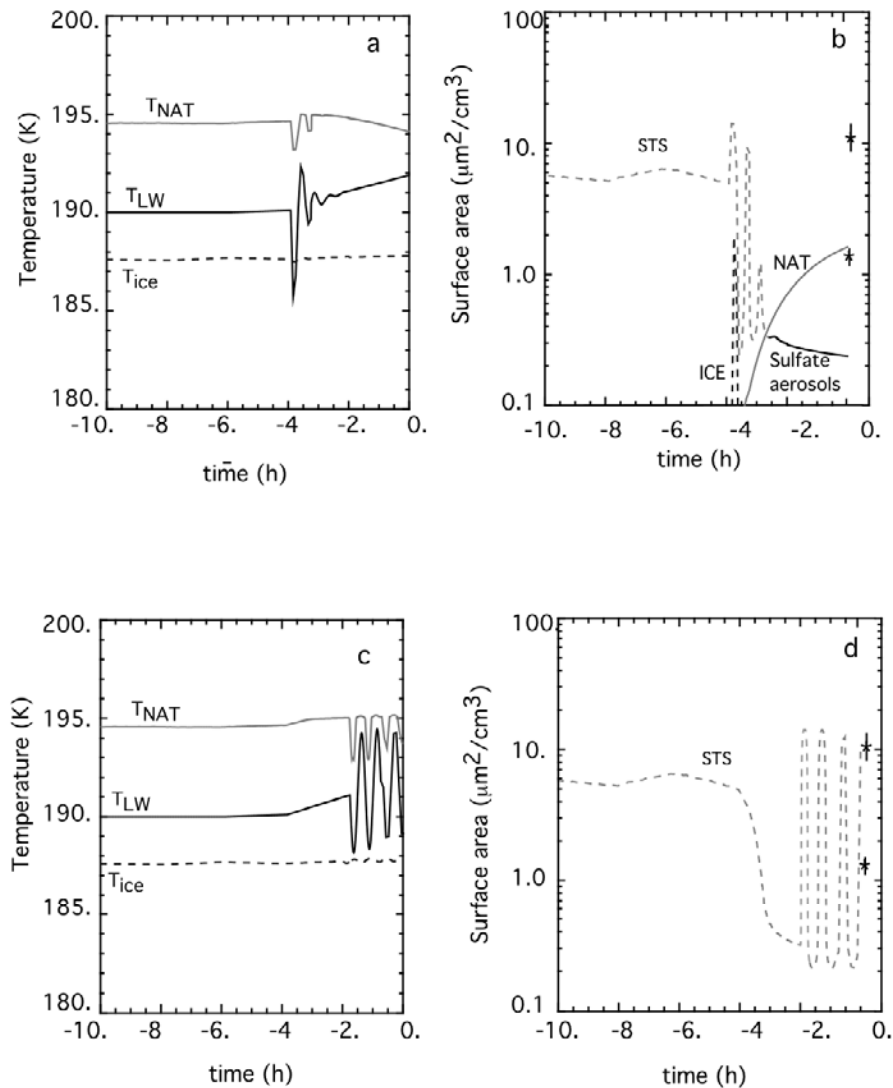


Figure 6. (a and b) Same as in Figures 4a and 4b but for T_{LW} s including temperature perturbation due to lee-wave event in the case of temperature history 1 (TH1). Only the last 10 hours of simulation before the measurements are presented. (c and d) Same as in Figures 4a and 4b but for T_{LW} s including temperature perturbation due to lee-wave event in the case of temperature history 2 (TH2).

that two types of particles contribute to the signal: the first type is a mode of medium-sized particles and the second type is a mode of larger non spherical particles. On the other hand, by using two temperature histories, the MiPLaSMO model predicts the existence of three types of particles: two of them (small liquid and NAT particles) coexisting in the region close to the balloon, and the third one (STS particles) existing alone in a region far from the balloon. The surface areas obtained by microRADIBAL for spherical particles and nonspherical particles are comparable to those calculated by MiPLaSMO for STS and NAT particles respectively.

[55] These results suggest us that microRADIBAL has detected signals coming from two regions associated with two types of particles, that differ in their location and formation processes. In fact, the two types of particles observed by microRADIBAL might be either mixed or in different locations since microRADIBAL is unable to distinguish between these two situations.

[56] We have been further in the comparison by plotting the size distributions derived from microRADIBAL measurements and the size distributions retrieved from modeling results with MiPLaSMO by using TH1 and TH2 (Figure 7). The predicted size distributions for STS and NAT are within the range of the measured size distributions for spherical and nonspherical particles. For these two types of particles, the median radius obtained with MiPLaSMO corresponds approximately to the upper limit given by microRADIBAL and the number of particles for MiPLaSMO corresponds to the smaller limit given by microRADIBAL.

[57] Concerning the sulfate aerosols particles predicted by MiPLaSMO using TH1, they cannot be detected by microRADIBAL because they are small ($r_{\text{eff}} \approx 0.05 \mu\text{m}$) and their number density is only about 10^3 times the number density of NAT particles, so their contribution to the signal is hidden by the contribution of the larger particles. Therefore, in addition to the agreement in measured and predicted surface area, as told previously, the

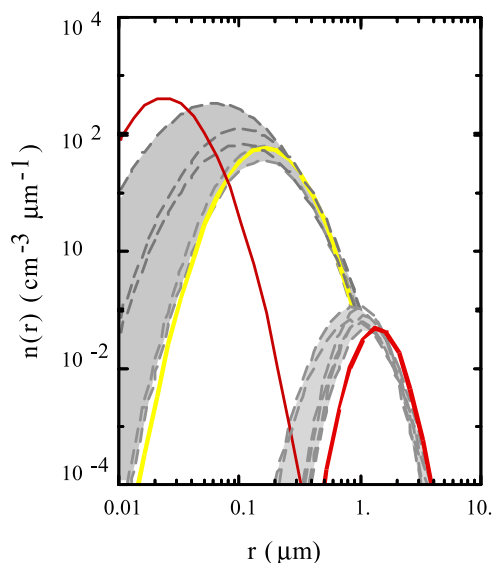


Figure 7. Size distributions measured by microRADIBAL at 20 km altitude (the gray areas cover all the size distributions (gray dash lines) obtained with the instrument, see Table 2), and size distributions obtained with MiPLASMO model: medium mode by using TH2 in yellow, small and large modes by using TH1 in red.

detailed information given by size distributions is also in rather good agreement.

[58] Measurements on this same day by Voigt *et al.* [2000] revealed also two types of aerosols located in two regions during the evening due to a lee-wave event. In this case, NAT and STS particles were formed successively in the same air mass, and did not coexist at the same time at the same location. The first type of particles was rather small, characterized by $r_{m1} = 0.05\text{--}0.25\ \mu\text{m}$ and concentration of about $15\ \text{cm}^{-3}$, the second type was larger, characterized by $r_{m2} = 0.5\text{--}1\ \mu\text{m}$ and concentration less than about $0.5\ \text{cm}^{-3}$. Therefore microRADIBAL PSC particle measurements are comparable in phase, liquid or solid, size and number density to those obtained by Voigt *et al.* [2000].

5. Conclusion

[59] MicroRADIBAL instrument has detected polar stratospheric cloud particles on 25 January 2000 at 10:00 UT, over northern Scandinavia at about 50 hPa. A detailed analysis of temperature history of the air masses combined with microphysical modeling shows that this PSC is associated with temperature perturbations due to lee-wave events. Detailed aerosol characteristics (size distribution, concentration, surface area density) have been extracted from measurements. An analysis over a large range of scattering angles, (excluding two features) accounting for the wavelength dependence of the signals, leads to an interpretation of the measurements in terms of two size distributions characterized by a medium mode corresponding to spherical particles and a large mode corresponding to non spherical particles. The MiPLASMO Lagrangian model has been run to tentatively explain the existence of such particles. Mountain wave-induced temperature amplitude

calculations, obtained with the NRL/MWMF model, have shown a large variability of the temperature perturbation amplitude depending on the location. Therefore two temperature histories have been deduced, leading to predicting three types of particles. The STS particles are associated with a small lee-wave event just before the measurements. Sulfate aerosols and NAT particles are obtained considering a stronger lee-wave event, where temperature decreased below T_{ice} , four hours before the time of measurement. The STS and NAT particles do not coexist in the same air mass at the same time.

[60] Surface areas of STS and NAT particles predicted by MiPLASMO are in good agreement with those of the medium-sized mode and of the large mode of particles measured by microRADIBAL. The measured and modeled particle size distributions (median radius, standard deviation and total number of particles) are also in agreement. Therefore the two modes of particles retrieved from microRADIBAL measurements might be identified as two types of particles, STS and NAT, existing in two geographical regions associated with two different temperature histories induced by lee-wave events.

[61] In this study, some microRADIBAL measurements have not been analyzed, they were probably due to microphysical processes that occurred at small scale. Additional investigations are needed, and could be based on a 3-D meteorological model including a detailed parameterization of PSC formation together with lee-wave prediction.

[62] **Acknowledgments.** The authors thank the balloon launch team of CNES (Centre National d'Etudes Spatiales) and the Swedish Space Corporation-Esrange. They are grateful to Terry Deshler (University of Wyoming) for providing his aerosol data, to Kenneth Carslaw (University of Leeds) for providing his deliquescence temperature calculation scheme, to Tabazadeh Azadeh (NASA Ames Research Center) for providing her parameterization of homogeneous freezing rates of NAD and NAT from nitric acid solutions, and to Michael Mishchenko (NASA GISS) for providing his T-Matrix code. The Naval Research Laboratory is acknowledged for giving access to POAM III data. This work has been supported by the Commission of the European Union (contract EVK2-CT-1999-0047) and by CNES and CNRS (Centre National de la Recherche Scientifique) within the French Program of Atmospheric Chemistry PNCA (contract 99CNES/358113). One author (SDE) acknowledges support for this research from The Office of Naval Research and from NASA's Atmospheric Chemistry Modeling and Analysis Program (ACMAP). SDE also thanks Paul Newman and Leslie Lait of NASA's Goddard Space Flight Center for access to the DAO assimilated data sets. The LOA thanks Christine Deroo for computational help. The anonymous reviewers are acknowledged for their careful and critical reading leading to a great clarification of the manuscript.

References

- Ackerman, M., et al., European validation of SAGE II aerosol profiles, *J. Geophys. Res.*, **94**, 8399–8411, 1989.
- Arvesen, J. C., R. N. Griffin, and B. D. Pearson, Determination of extraterrestrial solar spectral irradiance from a research aircraft, *Appl. Opt.*, **8**, 2215–2232, 1969.
- Bacmeister, J. T., P. A. Newman, B. L. Gary, and K. R. Chan, An algorithm for forecasting mountain wave related turbulence in the stratosphere, *Weather Forecasting*, **9**, 241–253, 1994.
- Berendt, A., Fernmessung atmosphärischer Temperaturprofile in Wolken mit Rotations-Raman-Lidar, Ph.D. thesis, Univ. Hamburg, Hamburg, 2000.
- Brogniez, C., R. Santer, B. S. Diallo, M. Herman, J. Lenoble, and H. Jäger, Comparative observations of stratospheric aerosols by ground-based lidar, balloonborne polarimeter and satellite solar occultation, *J. Geophys. Res.*, **97**(D18), 20,805–20,823, 1992.
- Brogniez, C., J. Lenoble, M. Herman, P. Lecomte, and C. Verwaerde, Analysis of two balloon experiments in coincidence with SAGE II in the case of large stratospheric aerosol amount: Post-Pinatubo period, *J. Geophys. Res.*, **101**(D1), 1541–1552, 1996.

- Brogniez, C., J. Lenoble, R. Ramanananahérisona, K. H. Fricke, E. P. Shettle, K. W. Hoppel, R. M. Bevilacqua, J. Hornstein, J. Lumpe, M. D. Fromm, and S. S. Krigman, Second European Stratospheric Arctic and Midlatitude Experiment campaign: Correlative measurements of aerosol in the northern polar atmosphere, *J. Geophys. Res.*, *102*(D1), 1489–1494, 1997.
- Carslaw, K. S., B. P. Luo, and T. Peter, An analytic expression for the composition of aqueous HNO_3 - H_2SO_4 stratospheric aerosols including gas-phase removal of HNO_3 , *Geophys. Res. Lett.*, *22*, 1877–1880, 1995.
- Carslaw, K. S., et al., Increased stratospheric ozone depletion due to mountain-induced atmospheric waves, *Nature*, *391*, 675–678, 1998.
- Carslaw, K. S., T. Peter, J. T. Bacmeister, and S. D. Eckermann, Widespread solid particle formation by mountain waves in the Arctic stratosphere, *J. Geophys. Res.*, *104*, 1827–1836, 1999.
- Cruzten, P. J., and F. Arnold, Nitric acid cloud formation in the cold Antarctic stratosphere: A major cause for the springtime ozone hole, *Nature*, *324*, 651–654, 1986.
- Deshler, T., and S. J. Oltmans, Vertical profiles of volcanic aerosol and polar stratospheric clouds above Kiruna, Sweden: Winters 1993 and 1995, *J. Atmos. Chem.*, *30*, 11–23, 1998.
- Deshler, T., B. J. Johnson, and W. R. Rozier, Balloon-borne measurements of Pinatubo aerosol during 1991 and 1992 at 41°N: Vertical profiles, size distribution, and volatility, *Geophys. Res. Lett.*, *20*, 1435–1438, 1993.
- Dörnbrack, A., T. Birner, A. Fix, H. Fientje, A. Meister, H. Schmid, V. E. Browell, and M. J. Mahoney, Evidence for inertia gravity waves forming polar stratospheric clouds over Scandinavia, *J. Geophys. Res.*, *107*(D20), 8287, doi:10.1029/2001JD000452, 2002.
- Eckermann, S. D., D. E. Gibson-Wilde, and J. T. Bacmeister, Gravity wave perturbations of minor constituents: A parcel advection methodology, *J. Atmos. Sci.*, *55*, 3521–3539, 1998.
- Fientje, H., A. Dörnbrack, A. Fix, and A. Meister, Airborne lidar measurements of polar stratospheric clouds above northern Scandinavia, paper presented at SOLVE-THESEO 2000 Scientific Workshop, Eur. Comm., NASA, Palermo, Italy, Sept. 2000.
- Frohlich, C., and J. London (Eds.), Revised instruction manual on radiation instruments and measurements, *WCRP Publ. Ser. 7*, *WMO/TD 149*, 140 pp., World Meteorol. Org., Geneva, 1986.
- Hamill, P., and O. B. Toon, Polar stratospheric clouds and the ozone hole, *Phys. Today*, *44*, 34–42, 1991.
- Herman, M., J. Y. Balois, L. Gonzalez, P. Lecomte, J. Lenoble, R. Santer, and C. Verwaerde, Stratospheric aerosol observations from a balloon-borne polarimetric experiment, *Appl. Opt.*, *25*, 3573–3584, 1986.
- Hertzog, A., F. Vial, A. Dörnbrack, S. D. Eckermann, B. M. Knudsen, and J.-P. Pommereau, In situ observations of gravity waves and comparisons with numerical simulations during the SOLVE/THESEO 2000 campaign, *J. Geophys. Res.*, *107*(D20), 8292, doi:10.1029/2001JD001025, 2002.
- Huret, N., E. D. Rivière, F. Taupin-Goffinot, and M. Pirre, Lagrangian study of polar stratospheric clouds: The role of lee wave events for clouds formation and chlorine activation at the end of February 1997 close to Kiruna, *Air Pollut. Res. Rep.* *69*, edited by K. S. Carslaw and G. T. Amanatidis, Eur. Workshop on Mesoscale Process. in the Stratos., Bad Tölz, Germany, 1998.
- Knudsen, B. M., J.-P. Pommereau, A. Garnier, M. Nunez-Pinharanda, L. Denis, G. Letrenne, M. Durand, and J. M. Rosen, Comparison of stratospheric air parcel trajectories based on different meteorological analyses, *J. Geophys. Res.*, *106*, 3415–3424, 2001.
- Koop, T., and K. Carslaw, Melting of $\text{H}_2\text{SO}_4 \cdot 4\text{H}_2\text{O}$ particles upon cooling: Implications for polar stratospheric clouds, *Science*, *272*, 1638–1641, 1996.
- Koop, T., K. S. Carslaw, and T. Peter, Thermodynamic stability and phase transitions of PSC particles, *Geophys. Res. Lett.*, *24*, 2199–2202, 1997.
- Larsen, N., Polar stratospheric clouds: Microphysical and optical models, *Sci. Rep. 00-06*, Dan. Meteorol. Inst., Copenhagen, 2000.
- Larsen, N., B. Knudsen, J. Rosen, N. Kjöme, R. Neuber, and E. Kyrö, Temperature histories in liquid and solid polar stratospheric cloud formation, *J. Geophys. Res.*, *102*, 23,505–23,517, 1997.
- Middlebrook, A. M., L. T. Iraci, L. S. McNeill, B. G. Koehler, M. A. Wilson, O. W. Saastad, M. A. Tolbert, and D. R. Hanson, Fourier transform-infrared studies of thin $\text{H}_2\text{SO}_4/\text{H}_2\text{O}$ films: Formation, water uptake, and solid-liquid phase changes, *J. Geophys. Res.*, *98*, 20,473–20,481, 1993.
- Mishchenko, M., L. D. Travis, and D. W. Mackowski, T-Matrix computations of light scattering by non spherical particles: a review, *J. Quant. Spectrosc. Radiat. Transfer*, *55*(5), 535–575, 1996.
- Ovarlez, J., and H. Ovarlez, Water vapor and aerosol measurements during SESAME, and the observation of low water vapor content layers, in *Polar Stratospheric Ozone, Proceedings of the Third European Workshop, Air Pollut. Rep. 56*, CEC Publ., Brussels, 1995.
- Pierce, R. B., et al., Large-scale chemical evolution of the Arctic vortex during the 1999/2000 winter: HALOE/POAM III Lagrangian photochemical modeling for the SAGE III-Ozone Loss and Validation Experiment (SOLVE) campaign, *J. Geophys. Res.*, *107*, 8317, doi:10.1029/2001JD001063, 2002 [printed 108(D5), 2003].
- Press, W. H., S. A. Teukolsky, W. T. Vetterling, and B. P. Flannery, *Numerical Recipes in FORTRAN*, 2nd ed., Cambridge Univ. Press, New York, 1992.
- Renard, J.-B., M. Chartier, C. Robert, G. Chalumeau, G. Berthet, M. Pirre, J. P. Pommereau, and F. Goutail, SALOMON: A new, light balloon-borne UV-visible spectrometer for nighttime observations of stratospheric trace-gas species, *Appl. Opt.*, *39*, 386–392, 2000.
- Rivière, E. D., et al., Role of lee waves in the formation of solid polar stratospheric clouds: Case studies from February 1997, *J. Geophys. Res.*, *105*(D5), 6845–6853, 2000.
- Santer, R., M. Herman, D. Tanré, and J. Lenoble, Characterization of stratospheric aerosol from polarization measurements, *J. Geophys. Res.*, *93*(D11), 14,209–14,221, 1988.
- Santer, R., C. Brogniez, M. Herman, S. Diallo, and M. Ackerman, Correlative measurements of the stratospheric aerosols, *J. Geophys. Res.*, *97*(D18), 20,825–20,835, 1992.
- Schreiner, J., C. Voigt, A. Kohlmann, F. Arnold, K. Mauersberger, and N. Larsen, Chemical analysis of polar stratospheric cloud particles, *Science*, *283*, 968–970, 1999.
- Steele, H. M., P. Hamill, M. P. McCormick, and T. J. Swissler, The formation of polar stratospheric clouds, *J. Atmos. Sci.*, *40*, 2055–2067, 1983.
- Tabazadeh, A., R. P. Turco, K. Drdla, M. Z. Jacobson, and O. B. Toon, A study of type I polar stratospheric cloud formation, *Geophys. Res. Lett.*, *21*, 1619–1622, 1994.
- Tabazadeh, A., E. J. Jensen, O. B. Toon, K. Drdla, and M. R. Schoeberl, Role of stratospheric polar freezing belt in denitrification, *Science*, *291*, 2591–2594, 2001.
- Toon, O. B., R. P. Turco, J. Jordan, J. Goodman, and G. Ferry, Physical processes in polar stratospheric clouds, *J. Geophys. Res.*, *94*, 11,359–11,380, 1989.
- Tsias, A., A. J. Prenni, K. S. Carslaw, T. P. Onasch, B. P. Luo, M. A. Tolbert, and T. Peter, Freezing of polar stratospheric clouds in orographically induced strong warming events, *Geophys. Res. Lett.*, *24*, 2303–2306, 1997.
- Voigt, C., et al., Nitric acid trihydrate (NAT) in polar stratospheric clouds, *Science*, *290*, 1756–1758, 2000.
- World Meteorological Organization (WMO), *Scientific Assessment of Ozone Depletion: 1998, Rep. 44*, Geneva, 1999.
- Zhang, R., M. T. Leu, and M. J. Molina, Formation of polar stratospheric clouds on preactivated background aerosols, *Geophys. Res. Lett.*, *23*, 1669–1672, 1996.

J.-Y. Balois, C. Brogniez, M. Herman, and C. Verwaerde, Laboratoire d'Optique Atmosphérique, Université des Sciences et Technologies de Lille, Bâtiment P5, F-59655 Villeneuve d'Ascq cedex, France. (jean-yves.balois@univ-lille1.fr; colette.brogniez@univ-lille1.fr; maurice.herman@univ-lille1.fr; christian.verwaerde@univ-lille1.fr)

S. Eckermann, E. O. Hulburt Center for Space Research, Code 7641, Naval Research Laboratory, Washington, DC 20375, USA. (eckerman@ismap4.nrl.navy.mil)

N. Huret, M. Pirre, and E. D. Rivière, Laboratoire de Physique et Chimie de l'Environnement, 3A Avenue de la Recherche Scientifique, Université d'Orléans, F-45071 Orléans cedex 2, France. (nhuret@cns-orleans.fr; mpirre@odyssey.cns-orleans.fr; emmanuel.riviere@cns-orleans.fr)

N. Larsen and B. Knudsen, Danish Meteorological Institute, Lyngbyvej 100, Copenhagen, Denmark. (nl@dmi.dk; bk@dmi.dk)